行政院國家科學委員會補助專題研究計畫 ☑成果報告 □期中進度報告

研發免標識即時超靈敏晶片應用到癌症指標分子之分析

計畫類別：☑個別型計畫　□整合型計畫
計畫編號：NSC 98－2113－M－009－017－MY3
執行期間： 98 年 8 月 1 日至 101 年 7 月 31 日

執行機構及系所：國立交通大學材料系/奈米科技研究所

計畫主持人：柯富祥

成果報告類型(依經費核定清單規定繳交)：□精簡報告　☑完整報告

本計畫除繳交成果報告外，另須繳交以下出國心得報告：
□赴國外出差或研習心得報告
□赴大陸地區出差或研習心得報告
☑出席國際學術會議心得報告
□國際合作研究計畫國外研究報告

處理方式：得立即公開查詢

中　華　民　國 101 年 8 月 6 日

中文摘要

我們在本三年期研究計畫支持下，已經有高品質與創新的成果產出。由新穎晶片的設計、製程方法、生物分子之測定應用等，均有突破性的成果。特別是在新的晶片設計研發上，我們的研究成果在2012年7月榮登美國化學會著名期刊ACS Applied Materials & Interfaces的封面故事，這是台灣首次有論文被此雜誌封面報導。本期末報告將就三年研究中的重要成果進形介紹，內容將包括(1)新穎的晶片研發；(2)研發出免標識即時超靈敏晶片，並應用到癌症指標分子之分析；(3)針對奈米金表面的蛋白質反應進行深入研究，以瞭解酵素在奈米表面之催化活性。

關鍵字：軟性電晶體，超靈敏晶片，酵素催化活性，不同尺度之奈米金，動力學表現，擴散暨碰撞理論。

Abstract

Thanks to the support of NSC three-year project, we have created some high quality and innovative research results. In the field of advanced chip design, manufacturing, and biochemical application, our research team gains fruitful finding. Our flexible chip research has been selected as the cover story on July 2012 from ACS Applied Materials & Interfaces, and this is the first contribution from Taiwan site on this famous journal. In this final report, we include three parts such as (1) pioneering chip design research; (2) silicon nanowire field-effect transistor (NWFET) that allows deoxyribonucleic acid (DNA) biosensing; (3) systematically analyze the effect of nanoparticle (NP) size on the catalytic behavior of enzyme–NP conjugates, and a shielding model based on diffusion–collision theory is developed to explain the correlation between the size effects and the kinetic responses.

Keywords: Flexible transistor, ultrasensitive chip, catalytic enzyme activity, effect of nanoparticle size, kinetic behavior, diffusion–collision theory.

(1) Pioneering chip design research

Introduction

New organic-polymeric materials and devices have recently been the focus of research in the field of nano-electrotechnology, primarily because of their resulting elastic properties compared to the properties of the individual constituents. These materials are widely pursued because they offer numerous advantages for developing flexible electronics, such as easy-processing, low-cost, low-temperature processing and easily implemented structure modifications. The use of various polymer materials as the dielectric layer in organic thin film transistors (OTFTs) has become a topic of interest, because they are produced using an inexpensive solution-phase process that is desirable for the planned commercialization of flexible OTFTs. Polymer dielectrics are very attractive for electronics applications because they exhibit good characteristics that can often be obtained simply by spin-coating, casting, or printing under ambient conditions. Organic and polymer materials have attracted considerable attention for the development of large-area, mechanically flexible electronic devices; therefore an inexpensive solution-phase processing method is desirable for the commercialization of OTFTs. These materials are widely pursued because they can be produced using many facile synthesis methods (e.g., spin-coating, dip-coating, printing, evaporation), they are highly compatible with a variety of substrates, including flexible substrates, and they present themselves the opportunity for structural modifications. Polymer materials with low dielectric constants (low-k) are known to decrease cross-talk noise and power dissipation, and when they are incorporated into device systems, they can dramatically decrease resistance-capacitance (R–C) delays. According to the International Roadmap for

Semiconductors (ITRS) guidelines, inter-metal insulating materials must have dielectric constants of approximately 2 to effectively obtain devices that are sized < 100 nm. There is currently a strong desire in the microelectronic industry to develop advanced, large-scale new composite polymer materials that can satisfy the growing demand for miniaturization with high-speed performance and flexibility. The goal is to develop an OTFT that has high mobility for certain semiconductor-polymer interfaces, which could be modulated to a very large extent. To be useful in technological applications, polymer films should have a morphology that either remains stable within an acceptable range of temperatures or undergoes a transformation that is controllable and predictable. However, searchers have had little success in developing new polymer low-k ultrathin films on flexible substrates at room temperature. Therefore, an investigation to determine the most suitable method for depositing the polymer thin films is needed; this method must consist of one or more distinct steps that can be performed at a low temperature.

In this study, we present for the first time an easy-to-follow chemical synthesis process for preparing new organic–organic P123–PS blend thin films for use as dielectric layers at low temperatures. This method provides a way to prevent the problem of pin-hole defects in pure ultrathin polystyrene film. The electrical properties of the P123–PS blend thin-film have been examined for advanced flexible MIM capacitor applications. The electrical insulating properties of a flexible MIM device prepared using an organic–organic P123–PS-blend thin film as a dielectric layer included low leakage current density and better capacitance density. In addition, the solution-processed-blend film acted as a gate dielectric for the fabrication of pentacene OTFT devices on flexible PI substrate, making them suitable candidates for use in future flexible devices as a stable gate dielectrics. We also tested the functionality of our OTFT device under tensile and compressive bending modes without any deterioration and sterile loss in its electrical performance. These new polymer blend dielectric materials have good stability when they are used in electronic devices as composite dielectric layers and give excellent results compared to other polymer dielectric materials.

Results and discussion

A capacitor (formerly known as condenser) is a passive two-terminal electrical component used to store energy in an electric field. The forms of practical capacitors vary widely, but all contain at least two electrical conductors that are separated by a dielectric (insulator). When there is a potential difference (voltage) across the conductors, a static electric field develops across the dielectric, thereby causing a positive charge to collect on one plate and a negative charge on the other plate. In practice, the dielectric between the plates passes a small amount of leakage current and has an electric field strength limit, resulting in a breakdown field. Electrical characterizations were performed to investigate the electrical insulation properties of the polymer blend film. Leakage current density-electric field (J–E) measurements were performed on the P123–PS blend thin film in a MIM structured device, as shown Figure 1(a) and the sample-image in Figure 1(b) to determine the leakage current characteristics and dielectric breakdown field. The J–E response is also used to determine the available range for high-quality capacitance density-voltage (C–V) measurements. First, we measured the insulator properties for the PS film. Note that the device performance was poor because the leakage current was very high (~10^{-4} A cm^{-2}) and the breakdown field was very low (< 1 MV cm^{-1}) because the film was affected by pinhole defects. However, the insulating properties were enhanced for the P123–PS film because this film was free of pinhole defects. Figures 1 (c) & (d) show typical J–E and C–V plots for the MIM configurations fabricated using the P123–PS blend thin-film as an insulator layer. As observed in Figure 1 (c),

the average low leakage current density value of the P123–PS film was estimated to be approximately 10–10 A cm^{-2} at an applied electric field between 5–10 MV cm^{-1}. The probe was moved to three different points ina random order on the P123–PS based MIM capacitor and exhibited leakage current values that were higher or lower than the average leakage current value and a good breakdown limit of the film. We examined the leakage current at three different points to determine the breakdown limit and the insulating quality of our film. The breakdown field for the P123–PS blend film was approximately 8.5 MV cm^{-1}. Based on this result, we concluded that the film is of very high quality and exhibited extremely good insulating properties. Figure 1(d) displays a characteristic C–V plot for P123–PS. As shown in Figure 1(d), the capacitance of the P123–PS blend film at three different points of 10KHz, 100KHz and 1 MHz are 88.2, 82.01 and 81.1 nF cm^{-2}, respectively. The J–E and C–V results demonstrated that the blend film generated using P123 and PS dissolved in organic solvents exhibit superior insulating properties compared to the corresponding neat polymers and many other previously reported materials.

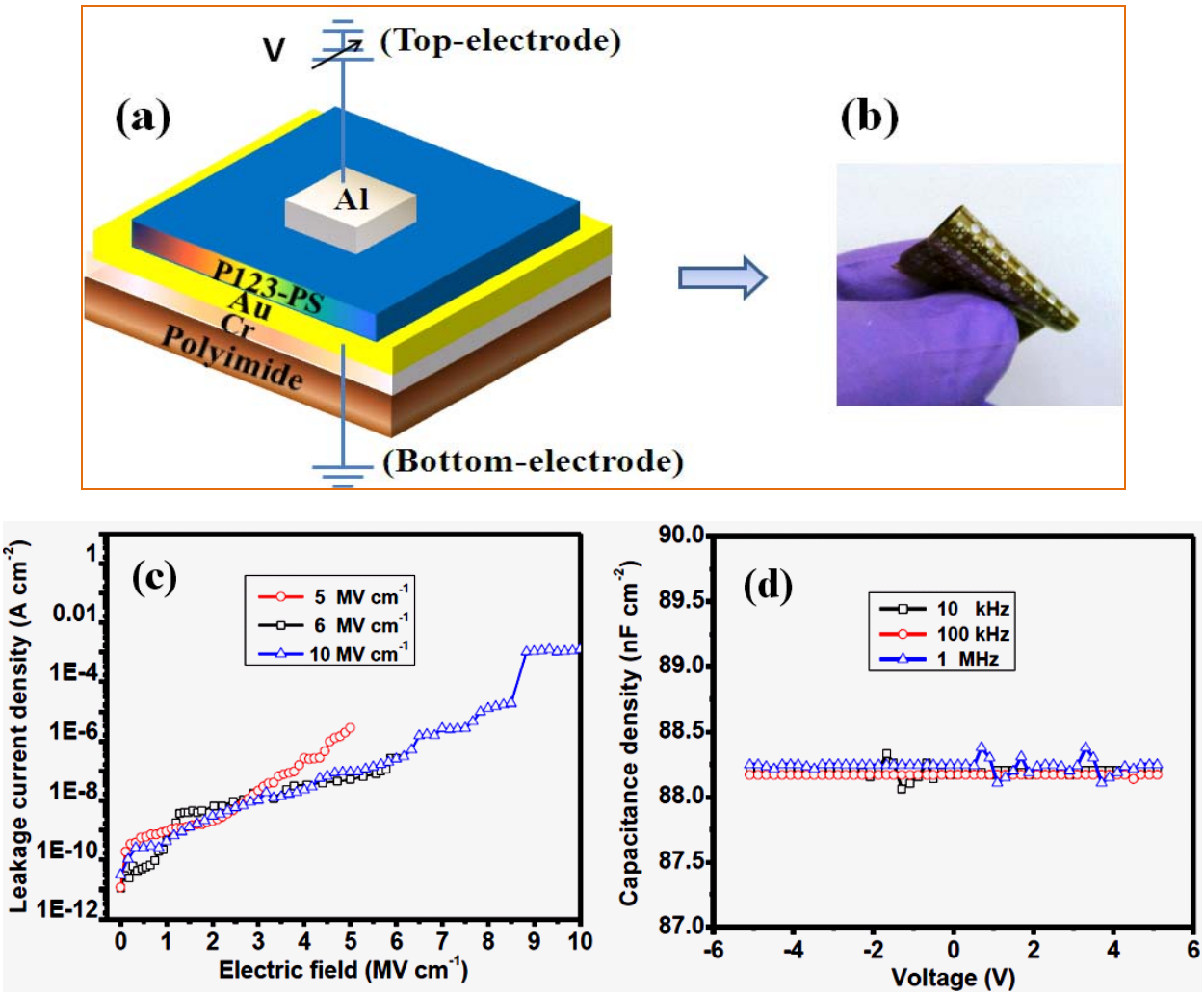

Figure 1 (a) Schematic view of the P123–PS blend thin film-based MIM capacitor; (b) photograph of a flexible MIM capacitors on area of 5×5 cm^2 on flexible PI substrate showing the sample bent by hand; (c) *J–E* and (d) *C–V* plots for MIM structured device fabricated using the P123–PS blend thin film as a gate insulator layer.

To demonstrate the performance of the polymeric P123–PS blend film as a dielectric layer, we fabricated a pentacene-based OTFT with the device geometry shown in Figure 2 (a); a sample image is shown in Figure 2 (b). Figure 2 (c) represents the drain current-drain voltage (IDS–VDS) output curve obtained from our OTFT that use P123–PS as a dielectric layer and pentacene as channel layer with a length (L)=70 µm and a channel width (W)=1500 µm. The device demonstrated desirable low-operating voltage p-type OTFT characteristics at an operating voltage of –5 V. The maximum saturation current of ~ 6.1×10^{-5} A was achieved at V_{GS} = –5 V. The observed OTFT characteristics both closely conformed to conventional transistor characteristics in the linear and saturation regimes to the drain current that increased linearly at low drain voltage and demonstraed clear saturation behavior at high drain voltage. The drain current-gate voltage (I_{DS}–V_{GS}) transfer curve of pentacene OTFT on P123–PS blend gate dielectrics (Figure 2 (d)) indicated that the OTFT yielded high current on/off ratios ($I_{on/off}$ =5×10^{5}) and negligible gate-sweep hysteresis.

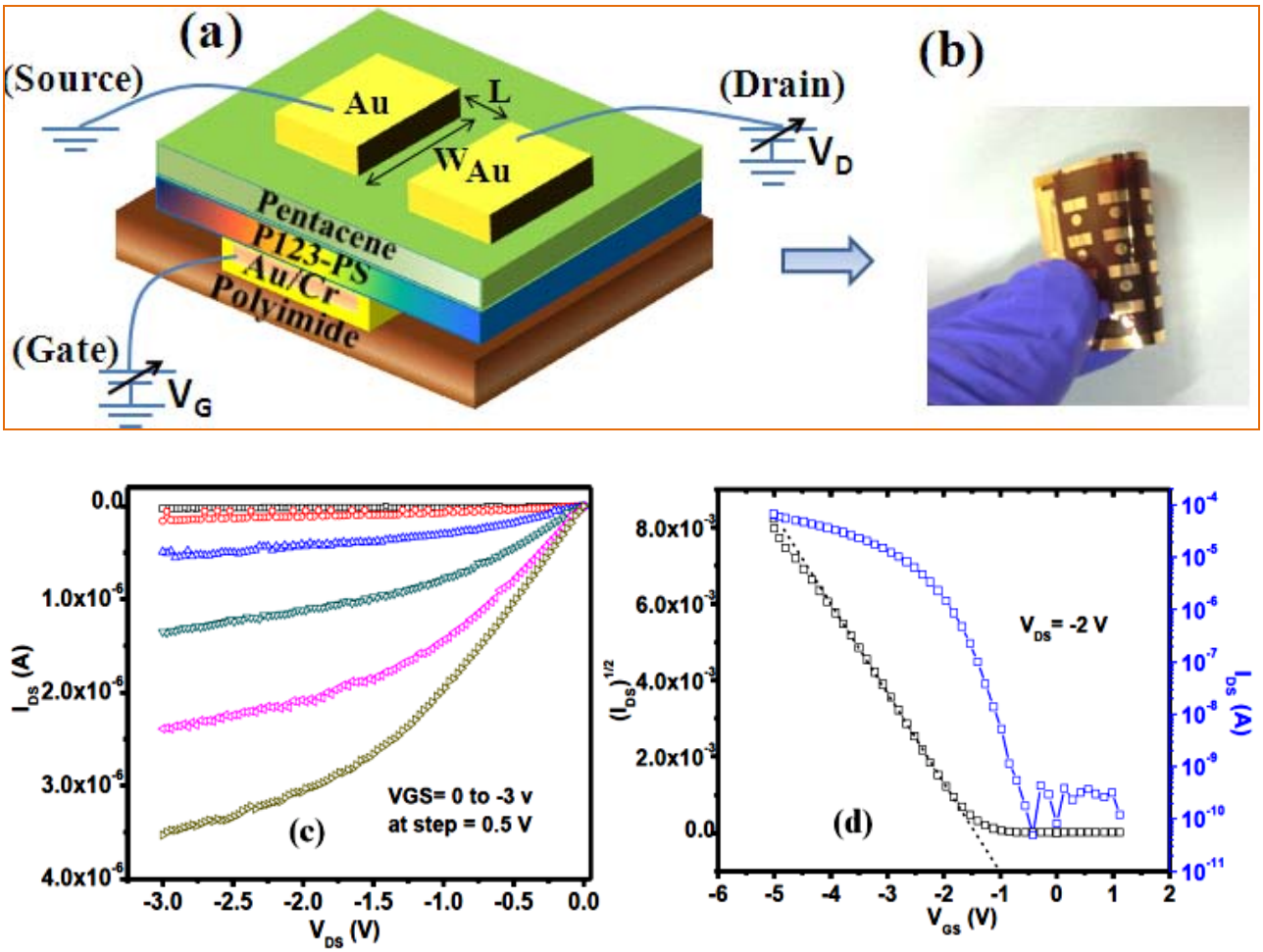

Figure 2 (a) Schematic representation of the OTFT device that features P123–PS as a gate insulator and pentacene as a semiconductor layer; (b) photograph of the OTFT devices on a 5×5 cm^2 area on flexible PI substrate and plots for the OTFT; (c) output characteristic (I_{DS}–V_{DS}), where V_{GS} ranges from 0 to –5.0 V at –1 V step, and (d) transfer characteristic (I_{DS}–V_{GS}), when V_{DS}= –2 V.

Conclusions

In summary, we developed an innovative approach for the deposition of a new organic-organic (P123–PS) blend thin film on a flexible polyimide substrate using a novel chemical dip-coating method at low temperature. The planar aggregation of pluronic EO20–PO70–EO20 triblock copolymer P123 and polystyrene materials is likely due to the strong assembly of hydrophobic and hydrophilic molecular interactions and high molecular weights. Due to the good insulating properties of our polymer blend film, it could be an ideal dielectric film for use in future in device applications. The time-induced contact angle measurement using water, ethylene glycol and diiodomethane for P123–PS revealed a good hydrophobic surface with a total surface free energy of 19.6 mJ m^{-2}. In addition, the polymeric P123–PS in a sandwich-like configuration (e.g., metal-insulator-metal) exhibits a low leakage current density value (~10–10 A cm^{-2}) and good capacitance density (88.2 nF cm^{-2}). An OTFT device employing P123–PS as a gate insulator and the conjugated π-electron system organic pentacene as a semiconductor layer was successfully constructed and exhibited excellent device performance (e.g., carrier mobility, 0.16 cm^2 V^{-1} s^{-1}; on-to-off current ratio, $5x10^5$) and good device stability. Furthermore, the performance of the OTFT device under bending modes of tensile and compressive strain are among the best results for these materials, which adopt a bottom-gate configuration; these results are attributed to the high-quality dielectric-organic semiconductor interface that was formed. Finally, it should be emphasized that this novel solution processed dip-coating method provides a new way to investigate the surface of polymeric blend films and could be a promising approach for practical applications because it is a low-cost and low-temperature manufacturing technique.

References

1 J. S. Meena, M.-C. Chu, Y.-C. Chang, C.-S. Wu, C.-C. Cheng, F.-C. Chang, F.-H. Ko*, Novel Chemical Route to Prepare a New Polymer Blend Gate Dielectric for Flexible Low-voltage Organic Thin-Film Transistor, ACS Applied Materials & Interfaces, v4, 3261-3260 (2012). [selected as the cover art of July issue]

2 J. S. Meena, M.-C. Chu, C.-S. Wu, J.-C. Liang, Y.-C. Chang, S. Ravipati, F.-C. Chang, and F.-H. Ko*, Facile synthetic route to implement a fully bendable organic metal-insulator-semiconductor device on polyimide sheet, Organic Electronics, v13, 721-732 (2012).

3 J. S. Meena, M.-C Chu, C.-S. Wu, F.-C. Chang and F.-H. Ko*, Highly reliable Si_3N_4-HfO_2 stacked heterostructure to fully flexible poly-(3-hexylthiophene) thin-film transistor, Organic Electronics, v12, 1414-1421 (2011).

(2) Silicon nanowire field-effect transistor for biosensing

Introduction

One-dimensional nanowires (NWs) are particularly appealing candidates for use in ultrasensitive miniaturized biomolecule sensors. Nanowire field-effect transistors (NWFETs) can suppress the short-channel effects encountered in nanoscale metal oxide semiconductor field-effect transistors and provide high surface sensitivity. Unlike the signal responses of conventional electrochemical cells operate based on the Nernst equation, the response of NWFETs featuring surface-immobilized molecules from the fluid is more complex. Recently, Nair and Alam (2008) derived a logarithmic relationship between the target molecular concentration and the electrical signal for an NWFET functioning based on the diffusion–capture model and the Poisson–Boltzmann equation. Silicon NWFETs have been fabricated using both "top down" and "bottom up" methods. The "bottom up" fabrication methods usually involve the formation of NWs through vapor–liquid–solid (VLS) growth, which is limited by the need for complex integration techniques that require precise transfer and positioning of individual NWs to provide reliable and superior ohmic contacts. In addition, control over the doping concentrations in self-assembled semiconducting nanostructures remains a great challenge, as is the fabrication of high-density sensor arrays. Furthermore, the use of an additional external gate—to precisely turn the NWFET sensor to higher sensitivity—is also critical. The "top down" methods for fabricating NWs usually employ the advanced lithography techniques used in the semiconductor industry, allowing mass-production with reduced fabrication costs. The excellent device performance and good ohmic contacts of such methods enable the possibility of integration. It has been reported that the presence of $BRAF^{V599E}$ mutation genes correlates to the occurrence of melanomas, colorectal cancers, gliomas, lung cancers, sarcomas, ovarian carcinomas, breast cancers, papillary thyroid carcinomas, and liver cancers. This mutation is believed to mimic phosphorylation in the activation segment by insertion of an acidic residue close to a site of regulated phosphorylation at serine 598. $BRAF^{V599E}$ exhibits elevated basal kinase activity and diminished responsiveness toward oncogenic stimulation. $BRAF^{V599E}$ also transforms NIH3T3 cells (murine embryonic fibroblasts) with higher efficiency than does the wild-type form of the kinase, consistent with the functioning as an oncogene. Therefore, characterization of the $BRAF^{V599E}$ mutation genes at the molecular level is significant for early tumor identification, allowing the possibility of aggressive and specific therapy to save human lives.

In this study, we used conventional complementary metal-oxide semiconductor technology to develop a 60-nm–wide Si NWFET that enables the sensing of mutated genes. We first evaluated various cleaning solutions for their use in improving the immobilization of DNA onto the silicon dioxide (SiO_2) surfaces, in terms of the fluorescence efficiency and the electrical properties of the sensors. We then applied the NWFET sensor as an ultrahigh-sensitivity molecular probe for the detection of a cancer-related $BRAF^{V599E}$ mutation gene.

Results and discussion

Figure 1 presents plot of the I_D–V_G at drain voltages (V_D) of 0.1 and 1 V, respectively, for the fabricated 60-nm NWFET biosensor. The current flowing through the NW located between the source and drain electrodes could be switched "on" and "off" at various backside gate potentials. If, at a large negative gate bias (e.g., –15 V), the channel conduction (ID) is very low, a positive voltage applied to the gate will create an n-channel (i.e., an electron carrier). Therefore, the sensor is a normally-on, n-channel depletion NWFET. In

general, a backside gate can apply a bias voltage to the NW and, thereby, affect the energy barrier for the charge carriers. This applied voltage ensures device operation under the optimal conditions of a larger current shift. Stern and co-workers (2007) proposed a p-channel DNA sensor with a backside gate control design; the sub-threshold swing (SS) for their device was, however, about 1250 mV/decade (I_D = 10^{-13} A and 10^{-9} A at -20 V and -25 V, respectively)—much higher than our value of 450 mV/decade. We attribute the high sensitivity of our DNA sensor to the use of the single crystal n-channel design rule having higher mobility and lower SS characteristic.

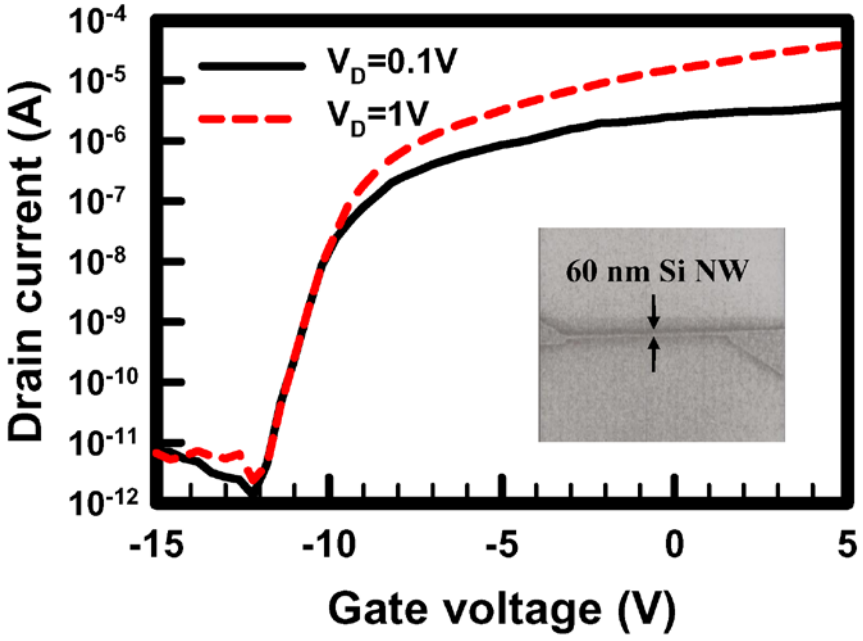

Figure 1 Plots of drain current versus gate voltage for the NWFET sensor, measured at values of V_D of 0.1 (black line) and 1 V (red dotted line). Inset: Scanning electron microscopy image of the 60 nm-wide Si NW.

To detect $BRAF^{V599E}$ mutation genes, we cleaned the surface of the NWFET with ACE and then immobilized a 30-mer capture DNA strand, having the sequence 5′-AAATATATTA-TTACTCTTGA-GGTCTCTGTG-3′, onto the surface. This capture DNA sequence is fully complementary to that of the target DNA which is partial sequence of the $BRAF^{V599E}$ mutation gene (Liao et al., 2009). Hence, the capture DNA on the NW surface formed a molecular probe for the detection of target DNA having the specific gene sequence 5′-CACAGAGACC-TCAAGAGTAA-TAATATATTT-3′. Figure 2(a) reveals the ability of the NWFET biosensors to detect cancer-related mutation genes. The threshold voltage for the capture DNA–modified NWFET, measured in PBS buffer solution, was –10.16 V (base line). Various concentrations of the target DNA, containing the $BRAF^{V599E}$ mutation gene, were adsorbed onto the surface of the NWFET device, providing a further rightward shift of the ID–VG curve, indicating the successful hybridization of the complementary mutation gene with the capture DNA. The fluorescence image in inset (I) confirms the successful hybridization of the 10 nM FITC-labeled target DNA to the capture DNA. For de-hybridization, we washed this dsDNA sample with hot DI (90 °C) to separate the target DNA from the probe surface; the curve returned to almost the same level as that of the base line. To ensure de-hybridization, we also used the FITC-labeled DNA to trace the reaction pathway of the molecule of

interest on the surface. The fluorescence image of the sample obtained after de-hybridization of the FITC-labeled target DNA [inset (II)] reveals that the target DNA was completely separated from the NW surface after de-hybridization. Figure 2(b) reveals the exponential relationship between the voltage shift of the NWFET sensor and the target DNA concentration. The voltage shift for the NWFET sensor under various target DNA concentrations of 10 fM, 1 pM, 100 pM, and 10 nM was 0.22±0.03, 0.45±0.05, 0.69±0.04, and 0.81±0.04 V, respectively. The relationship between the response of a nanobiosensor and the DNA concentration has been reported previously (Nair and Alam, 2008) to be

$$S(t) \propto \ln[\rho_0]$$

where S(t) is the sensor response, which is either a voltage or current shift, and is the DNA concentration. This equation suggests that the response of a nanoscale sensor should exhibit a logarithmic dependence on the DNA concentration, consistent with our finding. The linear fitting for the calibration curve is y = 0.119 * log(x) + 1.8817 from 10 fM to 100 pM with correlation coefficient of 0.988. The detection limit, which is defined as the minimal mutation gene concentration that gives a voltage shift which is 3 times the standard deviation, is estimated to 0.88 fM from the calibration curve. In addition, the relative standard deviation of threshold voltage shift for the target DNA is less than 12%.

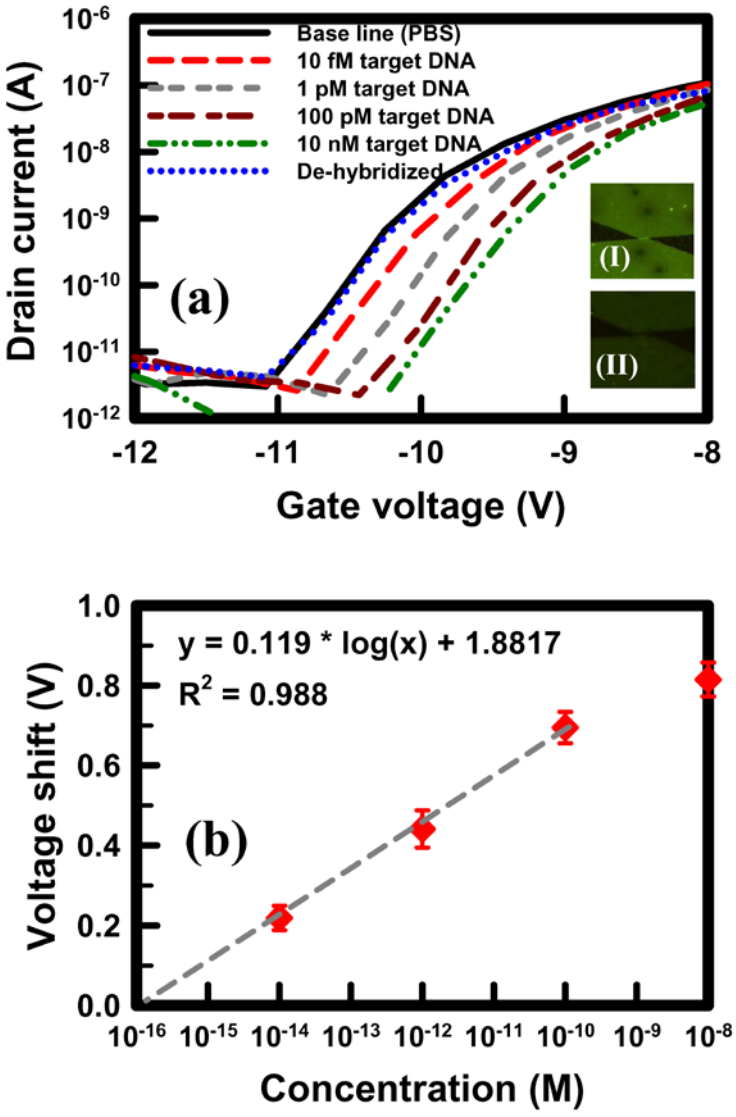

Figure 2 (a) Concentration-dependent electrical response of the capture DNA–modified NWFET sensor when detecting target DNA. The I_D–V_G curve of the base line was obtained in PBS buffer (black line); PBS buffer solutions containing target DNA at various concentrations (10 fM, 1 pM, 100 pM, 10 nM) were injected, respectively, and the I_D–V_G curves recorded. The de-hybridized samples were obtained after treatment of the dsDNA with hot DI water (90 °C); the ID–VG curves were then measured (red dotted line). Inset (I): Fluorescence image of 10 nM FITC-labeled target DNA bound to the capture DNA. Inset (II): Fluorescence image of the FITC-labeled target DNA after de-hybridization. (b) Voltage shift (from n=4) of the NWFET sensor plotted with respect to the target DNA concentration.

Figure 3 reveals the specific detection of target DNA using our NWFET. We investigated the behavior of mismatched target DNA strands (concentration: 10 nM) containing one and five mismatched bases; their DNA sequences were 5´-CACAGAGACC-TCAAGTGTAA-TAATATATTT-3´ and 5´-CACAGAGACC-TCAAGTACGG-TAATATATTT-3´, respectively. The latter exhibited the same response as that of the base line, whereas the former exhibited a rightward shift but could still be distinguished from the complementary sample. These results suggest that the single-base–mismatched target DNA hybridized to a small degree, but the five-base–mismatched DNA barely reacted with the capture DNA. A similar result has been reported for three-base–mismatched mutant genes, which interacted nonspecifically with an NW sensor, but could be quantified and distinguished from their corresponding wild-type genes (Hahm and Lieber, 2004).

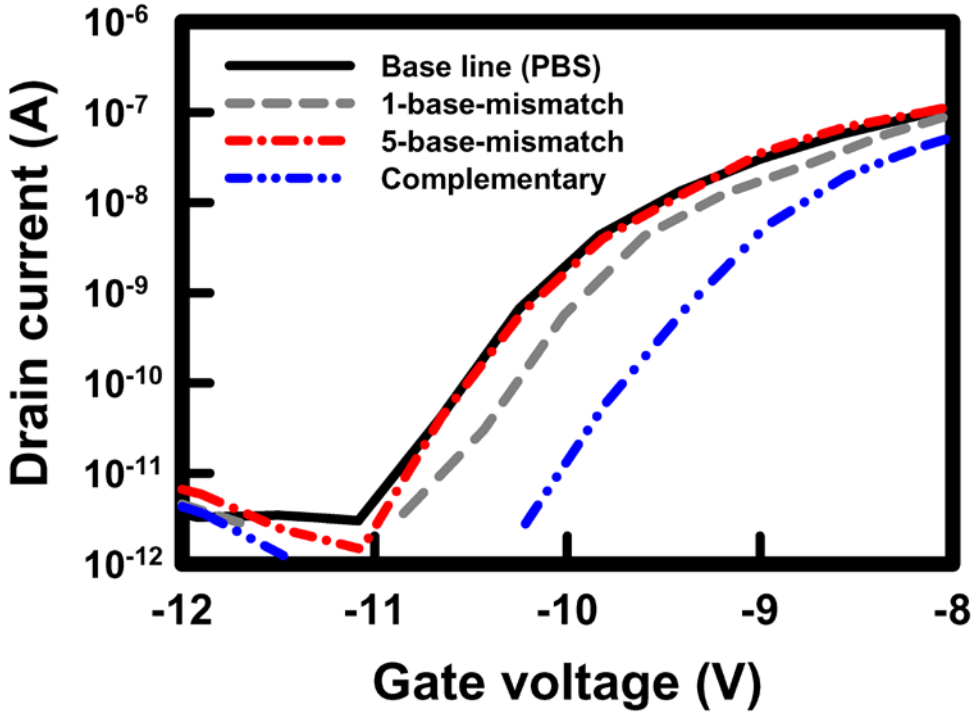

Figure 3 Electrical response of the capture DNA–modified NWFET sensor when detecting mismatched target DNA. The I_D–V_G curve of the base line was recorded in PBS buffer (black line); PBS buffer solution containing one- or five-base–mismatched target DNA strands (10 nM) was injected and the I_D–V_G curves were recorded.

Conclusions

Using a cleaning solution prepared from a mixture of acetone and ethanol allowed us to develop an NWFET device that behaved as a biomolecular sensor for an oncogene. We used the state-of-the-art semiconductor line to fabricate label-free NWFET devices having line widths of 60 nm. Connecting the NWs to source and drain electrodes fabricated on the SOI wafer provided functioning ohmic contacts without the problem of contact resistance. The NWFET exhibited n-channel depletion characteristics that allowed detection of the hybridization and de-hybridization of a $BRAF^{V599E}$ mutation gene from a cancer cell, as well as the ability to distinguish between complementary and mismatched target DNA. The detection limit of the NWFET biosensor for the sensing of the mutation gene was in the sub-femtomolar regime. Because this label-free NWFET sensor displayed the ability to detect the oncogene, such devices are potentially useful tools for biological research and genetic screening.

References

1 C.-C. Wu, F.-H. Ko*, Y.-S. Yang, D.-L. Hsia, B.-S. Lee, and T.-S. Su, Label-free biosensing of a gene mutation using a silicon nanowire field-effect transistor, Biosens. Bioelectron., v25, 820-825 (2009).

2 C.-C. Lin, F.-H. Ko*, C.-C. Chen, Y.-S. Yang, F.-C. Chang, C.-S. Wu, Miniaturized metal-semiconductor-metal photocurrent system for biomolecular sensing via chemiluminescence, Electrophoresis, v30, 3189-3197 (2009).

3 C.-C. Wu, T.-M. Pan, C.-S. Wu, L.-C. Yen, C.-K. Chuang, S.-T. Pang, Y.-S. Yang, F.-H. Ko*, Label-free Detection of Prostate Specific Antigen Using a Silicon Nanobelt Field-effect Transistor, Int. J. Electrochem. Sci., v7, 4432-4442 (2012).

(3) The effect of nanoparticle (NP) size on the catalytic behavior of enzyme–NP conjugates

Introduction

Many biomolecules, such as membrane proteins, perform their specific biorecognition or biocatalytic events while immobilized on the surfaces of cells or organelles. Several artificial technologies (e.g., bioconversion, bioremediation, biosensing) also take advantage of immobilized biomolecules and bio-species. In this regard, the modification and immobilization of enzymes has been studied widely for the generation of biocatalysts exhibiting enhanced stability and selectivity. Several synthetic scaffolds and supports, including gels, macromolecules, planar surfaces, and nanocomposites, have been used to immobilize enzymes. Among them, nanoparticles (NPs) provide an almost ideal mix of properties—minimum diffusional limitation, maximum surface area and high effective enzyme loading—to optimize the performance of immobilized enzymes while harnessing the fluorescent, magnetic and interfacial behavior of the resulting nanomaterials. However, studies of the effects of a NPs size, shape and material properties on both the kinetic experiments and theoretical model of the catalytic reactions of its enzyme–NP conjugates still remain rare.

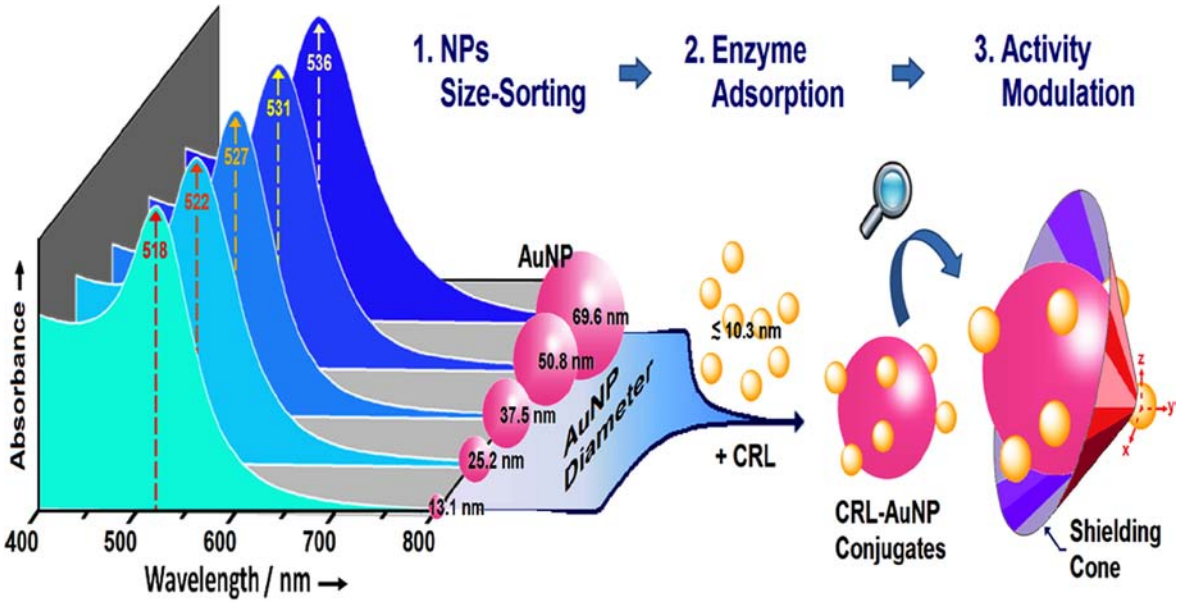

Scheme 1 Schematic representation of the preparation of CRL–AuNP conjugates that modulate the activity of the enzyme, and a cartoon of the shielding model.

In a previous paper, we demonstrated that adsorbing lipase onto gold NPs (AuNPs) significantly increased its enzymatic activity. In further investigations, we observed that the size of the NPs affected the catalytic activity; based on a diffusion–collision theory, we have attempted to develop a length-scale–dependent model to explain the effect of NP size on the modulation in activity of the enzyme–AuNP conjugate systems. In Nature, controllable modulation of enzyme activity is a potent means of regulating several cellular processes (e.g., signal transduction, biosynthesis, metabolism). The modulating of biocatalytic behavior is an attractive feature for exploitation in the field of nano-biotechnology. For extended studies of biocatalysis, lipases are very suitable esterases because of their well-defined structures, properties,

and applications. Lipases are used industrially in detergents, in paper and food technology, in the preparation of specialty fats, in various clinical studies, and for drug delivery. Therefore, in this study we selected Candida rugosa lipase (CRL, E.C. 3.1.1.3) to construct our enzyme–NP conjugates. As illustrated schematically in Scheme 1, we reported a series of experiments and a theoretical model designed to analyze the effect of AuNP size on the modulation of enzyme activity.

Results and discussion

We selected AuNPs as the adsorption materials for CRL in this study because they can be synthesized in a variety of diameters (13–100 nm) and readily characterized using UV–Vis spectrophotometry and scanning electron microscopy (SEM). In these experiments, we used a standard chemical reduction method to prepare spherical AuNPs having mean diameters of 13.1, 25.2, 37.5, 50.8, and 69.6 nm, under conditions that ensured their stability and lack of aggregation (see ESI I). For the preparation of enzyme-functionalized AuNPs with their colloidal stability, we performed the salt-induced colloidal tests to analyze the enzyme coverage and concentration of protection factor (C_p; see ESI II), determined by measuring the ratios of the absorbance at 620 nm (A_{620}) to those of the absorption signals (A_{peak}) of the differently sized AuNPs. To analyze the enzyme coverage, we define R as the ratio A_{peak}/A_{620}. When the enzyme concentration was sufficient to cap the AuNPs completely, R remained constant over time (i.e., no aggregation). In contrast, significant decreases in R occurred (i.e., aggregation) when the enzyme content was insufficient. We define the coverage as the ratio $(R - R_{min})/(R_{max} - R_{min})$, where R_{max} and R_{min} are the ratios (A_{peak}/A_{620}) in the presence of sufficient enzyme to provide colloidal stability and in the absence of enzyme (i.e., fully aggregated), respectively. Fig. 1 reveals the quantitative relationship between the percentage coverage of the AuNPs of various sizes and the CRL concentration; the values of C_p are determined at 50% coverage.

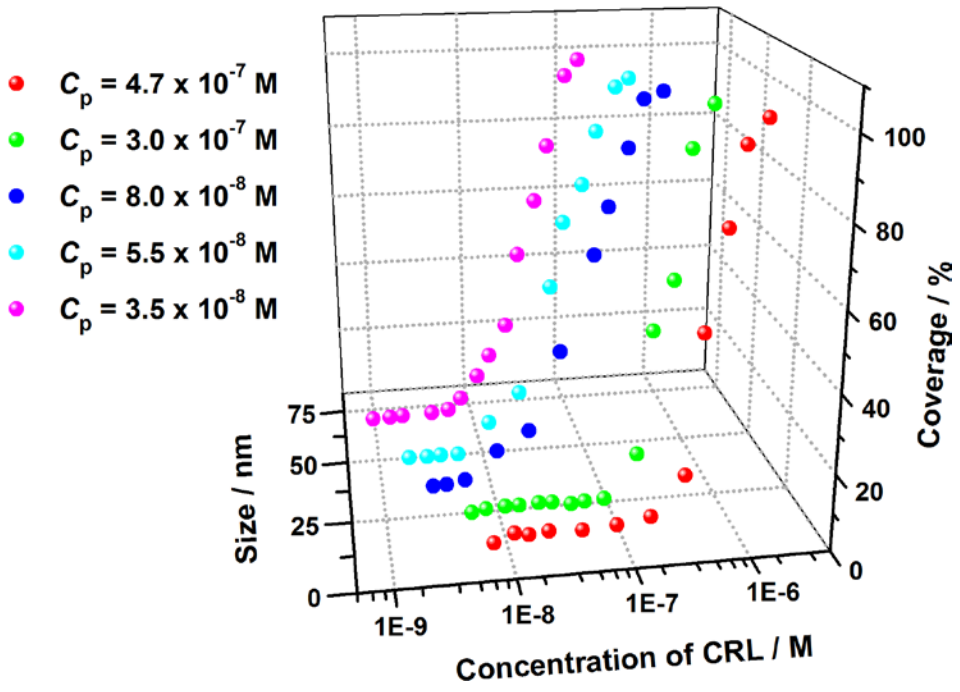

Figure 1 Coverages of the differently sized AuNPs plotted with respect to the CRL concentration. Color scheme: red, green, blue, light blue, and pink represent AuNPs having mean diameters of 13.1, 25.2, 37.5, 50.8, and 69.6 nm, respectively.

For the preparation of CRL–AuNP conjugates, the sufficient concentration of CRL (10-fold C_p of each set of CRL–AuNP complexes) was mixed with the AuNP solution of various sizes to ensure colloidal stability. The functionalized conjugates were washed repeatedly using centrifugation to remove excess enzyme. To assure that all unbound CRL was removed from the colloidal suspensions, activity tests were performed on the supernatants from the centrifugation/washing procedure. Table S1 (in ESI III) shows the drop in activity to zero as the conjugates are repeatedly cleaned. This procedure was repeated six times until no activity was measured to ensure the absence of free CRL in the systems. To detect the CRL loading on the AuNPs, KCN was used to oxidize and dissolve the AuNPs, thereby liberating the bound CRL from the surfaces of the conjugates. For AuNPs having mean sizes of 13.1, 25.2, 37.5, 50.8, and 69.6 nm, the enzyme concentrations were 104.3 ± 3.2, 61.7 ± 0.8, 16.5 ± 0.6, 11.0 ± 0.1, and 6.8 ± 0.1 nM, respectively. These values were reported for the activity assays of various CRL–AuNP conjugate systems. Using UV–Vis spectrophotometry, we detected the activities of the CRL–AuNP conjugates by measuring the absorbance of p-nitrophenol (pNP), a hydrolysis product from pNPP, at 405 nm. We observed that the initial release of pNP was proportional to the reaction time of various CRL–AuNP conjugated systems; in the insert of relative activity, there was a significant increase in the catalytic activity in the system featuring the smaller NPs, revealing that the size of the AuNPs was an important factor for the modulation of enzyme activity.

In the enzymatic kinetics experiment, Michaelis–Menten plots for the hydrolysis of *p*NPP (5.55–133.33 μM) catalyzed by the CRL–AuNP conjugates incorporating AuNPs of various average sizes were displayed in Fig. S9 (see ESI VI); the experiment-measured catalytic parameters were listed in Table 1. Although the turnover numbers k_{cat} for the various-sized AuNPs were similar, the Michaelis constants K_m for the smaller AuNPs had lower values. In previous studies, we found that the kinetics of the enzyme immobilized on one side of a planar surface could be effectively modeled and measured; in Table 1, when varying the AuNPs' dimensions, the values of K_m displayed an increasing trend in the presence of larger AuNP size, even under the extreme condition of AuNP size $\rightarrow \infty$. In simple terms, the rate constants for the individual steps were described in equation (eq.):

$$E_{NP} + S \underset{k_{-1}}{\overset{k_1}{\rightleftharpoons}} E_{NP}\text{-}S \xrightarrow{k_{cat}} E_{NP} + P \qquad \text{eq1}$$

An obtained lower value of K_m $[(k_{-1} + k_{cat})/k_1]$ represented greater kinetic affinity between the enzyme and the substrate; i.e., the conjugated system with the smaller AuNPs exhibited enhanced kinetic affinity, thereby improving the catalytic efficiency k_{cat}/K_m.

To further correlate the NP dimensions (size effect) to the catalytic efficiency (k_{cat}/K_m) of the conjugated enzyme, we developed a shielding model based on diffusion–collision theory (a detailed derivation is given in the ESI p14, theoretical considerations). We made the following assumptions: (i) the NPs, enzymes, and substrate molecules behaved as "rigid balls" (cf. Fig. 2); (ii) the intrinsic properties of the enzymes conjugated onto the differently sized NPs were similar; and (iii) the orientation of the active site of the enzyme–NP conjugates was random. Without considering multistep reactions, the catalytic reaction of substrate *S* with the conjugated enzyme E_{NP} can be approximated as the bimolecular reaction (Fig. 2 (a)) in eq. (2).

$$E_{NP} + S \rightarrow E_{NP} + P \qquad \text{eq2}$$

The reaction rate ν (μM s^{-1}) can be expressed as the product of the bimolecular rate constant k_{E-NP}^{coll} (μM^{-1}

s^{-1}) and the concentrations of the enzyme (C_E) and substrate (C_S), as in eq. (3).

$$v = k_{E-NP}^{coll} C_E C_S \qquad \text{eq3}$$

Relative to the free enzyme in solution, the E_{NP} provided additional steric hindrance for the binding of the substrate to the enzyme. We defined the shielding factor η as the solid-angle ratio of the enzyme surface exposed to substrate bombardment; the open solid-angle fraction Ω was displayed in Fig. 2 (c) with respect to the full solid angle 4π. Furthermore, combining diffusion–collision theory, the shielding effect (on the modulation of the probability of bombardment), and the Stokes–Einstein equation (the relationship between the diffusion coefficient and radius), we derived eqs. (4)–(6) to model the size effect:

$$k_{E-NP}^{coll} = Z \cdot p \cdot \eta \cdot e^{(-\frac{E_{act}}{RT})} = k_{max}^{eff} \cdot \eta \cdot e^{(-\frac{E_{act}}{RT})} \qquad \text{eq4}$$

$$k_{max}^{eff} = \frac{RT}{1500\mu}\left(\frac{1}{r_{NP} + 2r_E} + \frac{1}{r_S}\right)(r_E + r_S) \qquad \text{eq5}$$

$$\eta = \frac{\Omega}{4\pi} = \frac{1}{2}\left[1 + \frac{\sqrt{r_E(2r_{NP} + r_E)}}{r_{NP} + r_E}\right] \qquad \text{eq6}$$

where Z (μM^{-1} s^{-1}) was the frequency of collisions; p was the fraction of substrates that were in the correct orientation; E_{act} was the activation energy; R was the gas constant; and T was the absolute temperature; μ was the viscosity of the reaction mixture; k_{max}^{eff} (μM^{-1} s^{-1}) was the maximum frequency of effective collisions for the system (i.e., $\eta \rightarrow 1$ and $E_{act} = 0$); Ω was the solid-angle fraction of the enzyme surface open to substrates; r_{NP}, r_E, and r_S were the radii of the NP, enzyme, and substrate, respectively.

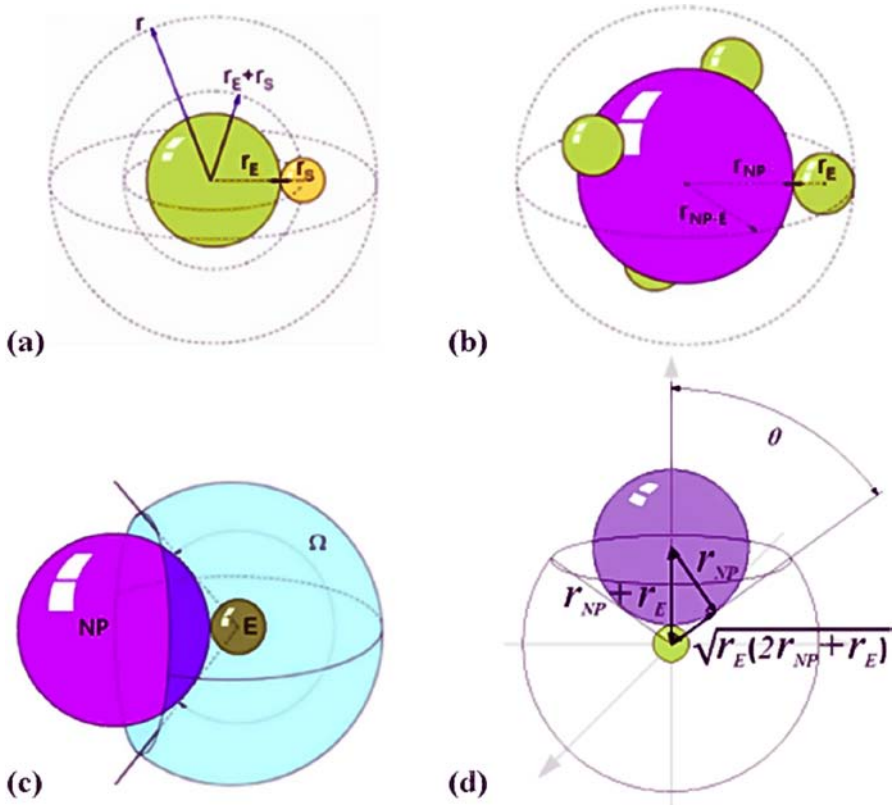

Figure 2 Geometric relationships between the substrate *S*, the enzyme *E* and the nanoparticle *NP*. (a) If the distance between the *S* and *E* was less than the sum of the radii of two bounding spheres, $r_E + r_S$, then a

collision event occurred. (b) Concerning diffusion effects in a fluid, the effective radius of the enzyme–NP conjugate should increase to $r_{NP} + 2r_E$. (c) The solid-angle fraction ▱ exposed for collisions between the substrate and the enzyme. (d) Geometric relationships of the respective radii.

Substituting the viscosity, absolute temperature, and radii (r_E = 5.17 nm; r_S = 0.58 nm; evaluated in the ESI, sections VII and VIII, respectively) into eqs. (4)–(6) gave the bimolecular rate constants k_{E-NP}^{coll} listed in Table 2. For the AuNPs having average diameters in the range 13.1 – 69.6 nm, the theoretical rate constants and the specificity constant kcat/Km (in Table 1) followed identical trends. In this model, when considering the extreme condition of $r_{NP} \rightarrow \infty$, the theoretical rate constant became 39.3% (0.48/1.22) of that for the system having a mean AuNP size of 13.1 nm. In comparison with the measured catalytic efficiency in Table 1, the enzyme immobilized onto a planar surface was 43.4% (0.82/1.89) of that of the system featuring AuNPs having a mean size of 13.1 nm. This percentage change was fairly consistent with the theoretical value. The enhanced activity by size-effect would theoretically converge to a finite maximum value when the AuNP size approached zero. Within the model of classical enzymatic kinetics, the shielding factor mainly affected the rate constant k_1, not k_{-1} or k_{cat} in eq. (1); that was, the steric hindrance affected only the binding path of the substrates, and not the desorption of the complex E_{NP}•S. Table 1 revealed that the values of k_{cat} were almost independent of the AuNP size, whereas the values of Km correlated strongly with it. Thus, this size-effect model had physical meaning and reasonably explained the kinetic response of this enzyme–NP conjugate system.

Conclusions

In summary, we had performed a series of experiments to systematically analyze the modulated NP size–dependent enzymatic activities of CRL–AuNP conjugates, and had developed a shielding model to explain the correlation between the size effects and the kinetic responses. A simple and efficient method for the preparation of this functional conjugates, with colloidal stability, under retention of enzymatic activity had been reported. The association of CRL with the AuNPs did not influence the values of k_{cat}, but the smaller AuNPs promoted the catalytic efficiency of CRL by increasing its kinetic affinity (i.e., lower K_m values) toward the substrate *p*NPP. In this study, we found that the sizes of these conjugates acted as a controllable and efficient factor for modulating the activity of the enzyme. We believed that as the integrative field of nano-biotechnology evolves, such studies of the fundamental interactions of nanostructures with biological systems will become, by necessity, more common.

References

1 C.-S. Wu, C.-C. Lee, C.-T. Wu, Y.-S. Yang and F.-H. Ko*, Size-modulated catalytic activity of enzyme–nanoparticle conjugates: a combined kinetic and theoretical study, Chemical Communications, v47, 7446-7448 (2011).

2 C.-S. Wu, F.-K. Liu, F.-H. Ko*, Potential role of gold nanoparticles for improved analytical methods: an introduction to characterizations and applications, Anal. Bioanal. Chem., v399, 103-118 (2011).

3 C.-C. Lee, H.-P. Chiang, K.-L. Li, F.-H. Ko, C.-Y. Su, and Y.-S. Yang, Surface Reaction Limited Model for the Evaluation of Immobilized Enzyme on Planar Surfaces, Anal. Chem., v81, 2737-2744 (2009).

國科會補助專題研究計畫成果報告自評表

請就研究內容與原計畫相符程度、達成預期目標情況、研究成果之學術或應用價值（簡要敘述成果所代表之意義、價值、影響或進一步發展之可能性）、是否適合在學術期刊發表或申請專利、主要發現或其他有關價值等，作一綜合評估。

1. 請就研究內容與原計畫相符程度、達成預期目標情況作一綜合評估

   ☑達成目標

2. 研究成果在學術期刊發表或申請專利等情形：

   論文：☑已發表 □未發表之文稿 □撰寫中 □無

   專利：□已獲得 □申請中 ☑無

   技轉：□已技轉 □洽談中 ☑無

   其他：（以 100 字為限）

3. 請依學術成就、技術創新、社會影響等方面，評估研究成果之學術或應用價值（簡要敘述成果所代表之意義、價值、影響或進一步發展之可能性）（以 500 字為限）

   過去三年在學們支持的三年期研究計畫，平均每年均有約 8 篇的論文被發表。研究以進行生化分子與奈米材料之反應機構研究，暨發展未來世代使用之超高靈敏光電感測器為主。我們研究軟性元件的製作方法，被美國化學會著名期刊 ACS Applied Materials & Interfaces 選為 2012 年 7 月榮登的封面故事，這是台灣首次有論文被此雜誌封面報導。另外在感測器製作方式與應用到癌症指標分子之分析上，我們自己設計元件與流體系統，以自行設計之晶片成功測定癌症的指標分子，此技術未來可以對台灣發展生醫科技有所助益。在生化分子與奈米材料之反應機構研究上，我們發展自組裝與微奈米結構形成方法，深入研究其合成之機構；另外酵素蛋白與奈米微粒之交互作用，我們就熱力學與動力學的角度研究調控酵素分子之活性與其影響之機制，瞭解到奈米微粒的選擇性反應，這些基礎性的研究均有高品質的成果發表。總體而言，這三年期的研究已經有許多原創性的學術與技術成果被提出，對於參與的研究團隊可以獲得許多寶貴的研究經驗，未來對於台灣工業界與學術界之發展定會有所幫助。

本三年期計畫每年均補助出國，第一及二年之出席報告均已在前兩年上傳到國科會，本處列出第三年計畫補助之心得報告。

國科會補助專題研究計畫項下出席國際學術會議心得報告

日期：100年 9 月25日

計畫編號	NSC 98－2113－M－009－017－MY3		
計畫名稱	研發免標識即時超靈敏晶片應用到癌症指標分子之分析		
出國人員姓名	柯富祥	服務機構及職稱	國立交通大學材料系/奈米科技研究所
會議時間	2011 年 9 月 14 日 至 2011 年 9 月 18 日	會議地點	匈牙利的首府布達佩斯
會議名稱	(中文)第 5 屆歐洲生醫工程國際會議 (英文)5th European Conference of the International Federation for Medical and Biological Engineering		
發表論文題目	(英文)Prostate Cancer Marker Sensing Under Nanostructural Biochip Technique		

一、參加會議經過與心得

第 5 屆歐洲生醫工程國際會議(5th European Conference of the International Federation for Medical and Biological Engineering)於 2011 年 9 月 14 日至 9 月 18 日在匈牙利的首府布達佩斯 (Budapest, Hungary) 舉辦，本會議每三年盛大舉辦一次，為歐洲聯盟最重要的生醫工程研究會議。根據大會提供的資料，第一屆會議於 1999 年於奧地利維有納舉行，第二屆於 2002 年於奧地利維有納舉行，第三屆於 2005 年於捷克布拉格舉行，第四屆於 2008 年於比利時的安特衛普舉行。本年度場地是在布達佩斯市近郊的世界貿易會議中心，其前方為著名的 Novotel 旅館，也是大會指定的住宿旅館。布達佩斯市的交通非常便利，有地鐵(Metro)、巴士(Bus)、街車(Tram)、火車(Train)等，因此很方便出外開會者利用大眾交通工具行動。另外布達佩斯市以多瑙河為中心，西邊稱為布達，而東邊稱為佩斯。由於大會的旅館相當貴，因此此行我的旅館位於地鐵 Batthyany 站附近，每天搭地鐵經 2 站後，再轉 Tram 經 3 站後，即到達會場。我於 9 月 2 日搭乘台北直飛德國法蘭克福的華航班機，9 月 3 日到 12 日為私人行程，9 月 13 日由法蘭克福國際機場搭乘德國航空班機直飛需匈牙利首都布達佩斯，並先走一趟會場以熟悉交通路線。9 月 14 日到會場報到並參加開幕，大會邀請兩位學者進行開幕的演講。我的演講在 17 日上午 8:45，18

日開會到中午，隨即下午搭乘德國航空飛回法蘭克福機場，在附近旅館住一晚後，搭乘中華航空 19 日中午的航班由法蘭克福直飛台北，9 月 20 日清早 06:25 到達桃園國際機場，隨即搭車回新竹。本次大會參加的人數超過 700 位，總計有 352 篇論文被發表，這些論文來自 61 個國家。由於論文數相當多，因此最多同時有四個場所發表論文。本人參與許多的演講活動及海報論文的討論，也對許多學者的研究留下深刻的印象。利如奧地利維也納大學分析化學系的 Dickert 教授，提出利用 QCM/SAW 的仿生感測器來應用到醫學及生物學上之生物粒子分析。可以測定 hormone、insulin、allergen、virus、cell、erythrocyte 等。東京醫學及牙醫大學的 Mitsubayashi 教授，則發展了軟性接觸透鏡，可以直接貼在眼睛上來測定淚液中的葡萄糖含量。長庚大學電子系的潘同明教授則發展高介電薄膜元件來測定酸鹼度及尿素濃度。本人發表的論文題目是 Prostate Cancer Marker Sensing Under Nanostructural Biochip Technique，論文發表時段是在週六上午 8:45-9:00 在 Brahms room。所發表的論文與本研究計畫有相當程度的相關，分別涵蓋奈米線場效電晶體來測定攝護腺癌標記蛋白，並於國外的學者專家有深入面對面之交流機會。本次會議參加的學者國籍達 61 國之多，大家的討論使得會場相當熱鬧，並同時碰到許多來自台灣的老師等。

附上一些參加本次會議的照片：

我發表的論文現場

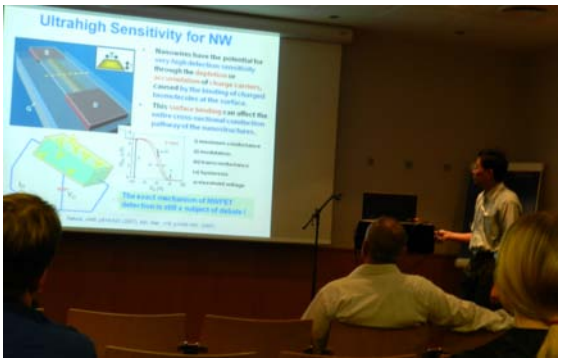

大會開幕的現場及大會演講

大會的報到處及會場外照片

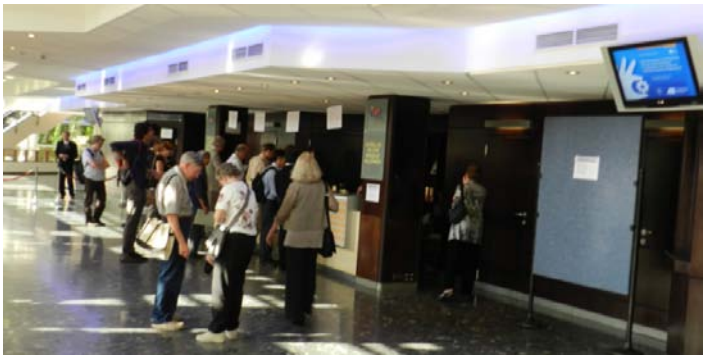

論文交流盛況

論文演講會場

海報論文發表現場

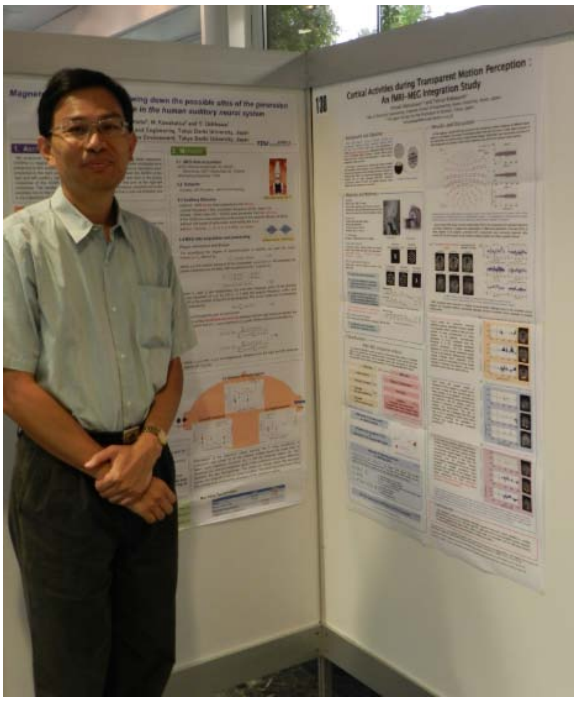

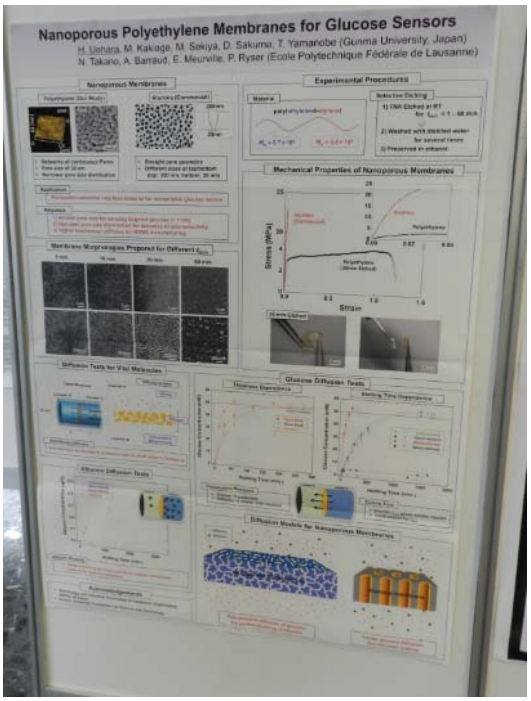

二、考察參觀活動

此行參加第 5 屆歐洲生醫工程國際會議並發表學術論文，雖然會議是 14 日才開始，但我於 13 日即提前一天抵達布達佩斯，除了預先查看會議場所外，也乘機參訪這座充滿歷史古蹟的布達佩斯城。這座城市擁有許多中世紀的史跡與建築，並顯出屬於馬札兒人的文化與藝術，利如蓋特勒丘陵、聖史蒂芬大教堂、國會大廈、英雄廣場、鎖鍊橋等。整座城市的所有建築均充滿中世紀的感覺，連正在修繕的公共場所，其施工非常仔細與考就，令人對於自 1990 年開始實施民主政治的這個國家覺得非常有前景。相較於西班牙或是義大利城市之混亂景像，匈牙利人民顯的十分純樸且客氣，而都市也十分有秩序，讓我對這個美麗且具有輝煌歷史的都市留下非常好的印象。另外匈牙利地鐵一號線(黃線)也是歐洲最古老的地鐵，所有的地鐵站與車箱充滿濃濃的歲月風。我也參觀布達佩斯市中心的中央市場，整個市場位在一座雕工令人相當驚嘆的建築物內，裏面販賣的均為當地人民例行的食物與衣物。

三、建議

參加此三年舉辦一次的歐洲生醫工程國際會議，發現除了許多感測器應用在分析外，也有其他生醫與資訊整合的系統被研究報導，由於目前全世界對於生醫領域應用在人類的生老病死非常重要，台灣科技界目前也往此趨勢之研究前進，台灣在電子領域具有全球的優勢，可以再進一步與生醫領域整合，將對台灣工業的未來會有相當之助益。

四、攜回資料名稱及內容

5th European Conference of the International Federation for Medical and Biological Engineering 論文集，並與國外學者交換 8 張名片。

五、其他

發表論文內容

Prostate Cancer Marker Sensing Under Nanostructural Biochip Technique

Abstract—A silicon nanobelt field effect transistor (SiNB-FET) device was proposed as an alternating platform of ultra-sensitive biosensor, and apply to the label-free detection and early diagnosis of the prostate specific antigen (PSA). The designed SiNB-FET molecule sensor demonstrated real-time, label-free, and high-selective properties in detecting biomole-cules. The novel back-gate SiNB-FET was fabricated by using the state-of-the-art complementary metal oxide semiconductor (CMOS) manufacturing technology. The shrank nanobelt structure with high surface-to-volume ratio and individual back-gate controlling was achieved by the local-oxidation of silicon (LOCOS) process. The probe molecule was sequentially immobilized onto the device surface for the purpose of target molecule sensing. Those molecules bearing with charge charac-teristics significantly influenced the charge carrier in the device channel. Hence, the target PSA can be easily detected from the shift of device's electrical property. In this research, the operating condition of device's gate controlling voltage was carefully studied. In addition, the molecular amplification method was developed to enhance the method's sensitivity. Finally, real samples from the hospital site were evaluated to characterize the concentration. We have demonstrated the detection capability of PSA by the SiNB-FET, and results show that the nanobelt biochip will be applied to the clinical diagno-sis, and verify its feasibility on the ultrasensitive diagnosis of prostate cancer in the future.